

Simulations of Strong Gravitational Lensing with Substructure

Adam Amara

Institute of Astronomy, Cambridge University, Madingley Road, CB3 0HA United Kingdom

and

R. Benton Metcalf¹

Department of Astronomy and Astrophysics, University of California, Santa Cruz, CA 95064 USA

and

Thomas J. Cox

Department of Physics, University of California, Santa Cruz, CA 95064 USA

and

Jeremiah P. Ostriker

Institute of Astronomy, Cambridge University, Madingley Road, CB3 0HA United Kingdom

ABSTRACT

Galactic sized gravitational lenses are simulated by combining a cosmological N-body simulation and models for the baryonic component of the galaxy. The lens caustics, critical curves, image locations and magnification ratios are calculated by ray-shooting on an adaptive grid. It is found that the simulations do not cause the observed number of violations of the cusp caustic magnification relation. A part of this may be due to an insufficient amount of substructure but even for unsmoothed simulations (with maximal substructure) the factor of three increase in the number of violations still did not match the data. This suggests that other factors play an important role. These may include lensing by structure outside the halo, selection bias and the possibility that a randomly selected galaxy halo may be more irregular, for example due to recent mergers, than the isolated halo used in this study. It is also shown that, with the computed level of substructure, the image magnifications of the Einstein cross type lenses are very weak functions of source size up to ~ 1 kpc. This is also true for the magnification ratios of widely separated images in the fold and cusp caustic lenses. This means that the magnification ratios for all the emission regions of a lensed quasar should agree with each other, barring microlensing by stars. The source size dependence of the magnification ratio between the closest pair of images is more sensitive to substructure. The ratios of image multiplicities are calculated. The ratio of four image to two image lenses is found to be $\sim 8\%$ for our elliptical galaxies and $\sim 40\%$ for our disk galaxies where there is also a $\sim 6\%$ chance of having a three image, naked cusp, lens.

Subject headings: gravitational lensing – cosmology: dark matter – galaxy:structure

¹Hubble Fellow

1. Introduction

Evidence has been mounting that there is a large amount of small scale structure in the distribution of matter in the gravitational lenses responsible for multiply images quasi stellar objects (QSOs) (Metcalf, 2004; Metcalf et al., 2004; Keeton et al., 2003; Metcalf & Zhao, 2002; Kochanek & Dalal, 2004; Dalal & Kochanek, 2002; Chiba, 2002; Metcalf & Madau, 2001; Mao & Schneider, 1998). The identity of this substructure is a matter of some debate. The Cold Dark Matter (CDM) model does predict that some substructure in the dark matter will survive within the halo of the lens galaxy. Mao et al. (2004) have argued that, according to Λ CDM (CDM with a cosmological constant) simulations, there is not enough surviving substructure in the central regions of halos of galaxies to account for previous lensing estimates. Metcalf (2004) has argued that, within the Λ CDM model, halos outside the lens galaxy will have enough of an effect to account for most of the observed lensing anomalies. It is important to determine just how important the substructure within the lensing galaxy will be. In this paper we address this question by studying the properties of a gravitational lenses taken directly from a cosmological simulation.

Five important methods have emerged for detecting substructure in a relatively model independent way. Initially, the simple magnification ratios were compared to predictions from a model for each lens (Chiba, 2002; Dalal & Kochanek, 2002) or a family of models (Metcalf & Zhao, 2002). This showed that most of the observed lenses are not consistent with the simple lens models that are usually used and that substructure was a probable explanation. Metcalf & Madau (2001) (also see Metcalf, 2001) predicted that the presence of substructure will cause changes in the image magnifications that are skewed differently for negative parity (saddle-point) images than they are for positive parity (minimum) images. Schechter & Wambsganss (2002) investigated this in the case of microlensing and Kochanek & Dalal (2004) showed that a sample of the observed QSO lenses do in fact show this tendency even at radio wavelengths. This is a property that is difficult to reproduce by any possible contaminating effect and it is relatively independent of the lens model used.

Mao & Schneider (1998) pointed out that lens M1422+231 violated the cusp caustic magnification relation. If the source is close enough to, and inside, a cusp in a caustic curve three of the images will be clustered together and the sum of their magnifications will be zero (taking the negative parity image to have negative magnification). Keeton et al. (2003) showed that this relation holds for a wide class of smooth, analytic lens models when three of the images are close enough together. They also showed that all known, and well observed, cases violate this relation although some of the cases might be due to microlensing by stars rather than larger mass substructures. Analyzing simulated galaxies Bradač et al. (2003) claimed that this relation can be violated without substructure if the lens has a stellar disk. In this paper we will revisit this question of how reliable the cusp caustic relation is and what kind of substructure can cause violations.

Another method for avoiding model dependence was proposed by Moustakas & Metcalf (2003) and was put into practice by Metcalf et al. (2004). In this approach the QSO magnification ratios are measured in several different wave bands. Since the sizes of the emission regions of a QSO are strongly dependent on wavelength (from $\lesssim 1000$ AU for the visible to hundreds of parsecs for the narrow emission lines) the magnification ratios could potentially be different if there is structure in the lens (or some where in front or behind the lens) at the size scales spanned by the regions observed. Metcalf et al. (2004) found that, among other things, the

mid-infrared, radio and narrow line magnification ratios are not consistent with each other and a lens without small scale substructure. A lower limit was put on the mass and density of substructures that could cause this mismatch. The reliability of this method rests on the requirement that the magnification ratios are not a strong function of source size. Metcalf et al. (2004) tested this assumption for a smooth analytic model of the lens used in that study, but here we will test it with more realistic lens models and in more generality (section 3.3).

The reliability of these methods for detecting substructure in gravitational lenses has only been verified in cases where the lens galaxy is represented by simple analytic models. The one exception to this is Bradač et al. (2003) where lenses were simulated using the hydrodynamic, galaxy formation simulations (Abadi et al., 2003; Meza et al., 2003). Bradač et al. (2003) investigated the cusp caustic magnification relation and the statistics of even/odd parity image magnification ratios. They found that the cusp caustic relation could be grossly violated for disk lens galaxies and that in the presence of substructures the caustics would develop a large number of “dove tails”. Their simulated galaxies were not entirely realistic because of limitations in the simulations. Most notably, the baryons and dark matter in their simulations are much more concentrated in the center than in real galaxies. This can potentially have a large effect on the lensing properties because the surface density at the location of the images is significantly smaller than what it would be in a real lens and a more concentrated mass distribution makes the potential more spherical at the distance of the Einstein ring. Our results will be compared to this work.

The paper is organized as follows. In section 2 the simulations are described in two parts starting with the galaxy simulations and then the lensing calculations. Section 3 has the lensing results broken down into several subsections. In section 3.1 we study the noise in the image magnifications caused by shot noise in the N-body simulations. In section 3.2 we look at the structure of the lensing caustics and the probabilities for different image multiplicities. The dependence of the magnification ratios on source size is addressed in section 3.3 and in section 3.4 the violations of the cusp caustic relation for our simulated lens are studied. A very brief comparison of these results with observations is given in section 3.5. A summary of the paper and a discussion of its wider implications are given in section 4.

2. Simulations

To test the effects substructure has on galactic lenses, we adopt a hybrid approach which implants an idealized model galaxy (either disk or elliptical) into the center of a dark-matter halo that has been extracted from a collisionless N-body simulation. The advantage of this approach lies in the fact that we are not limited by the inability of current numerical simulations to generate realistic galaxies. Conversely, the disadvantage is that the dark matter halo has been evolved to redshift zero without the dynamical effects of a baryonic galaxy. Below we describe how we attempt to overcome this fact.

For all idealized model galaxies considered here, we extracted the dark matter halo from the N-body simulation of Moore et al. (1999). This is a Milky Way size galactic halo and was simulated with a force resolution of ~ 0.5 kpc and contains 1,362,104 dark matter particles within 265 kpc, each with a mass of $1.68 \times 10^6 M_\odot$, which makes the total mass roughly $2.29 \times 10^{12} M_\odot$. The minimum resolved substructure (~ 50 particles) is approximately $8.4 \times 10^7 M_\odot$, which is a factor of 6 better than that of Bradač et al. (2003).

As mentioned above, we implant two idealized model galaxies into the center of our dark

matter halo. To conserve the total mass, we decreased the mass of all dark matter particles in accordance with the implanted baryonic mass. The first idealized galaxy is modeled after the early-type spiral lens galaxy Q2237+0305 (Trott & Webster, 2002). The total baryonic mass implanted is $2.5 \times 10^{11} M_{\odot}$, of which 71% is in an exponential disk with a scale radius of 9.5 kpc, and the remaining 29% is in the form of a Hernquist (1990) bulge, of effective radius 7.0 kpc. The resulting circular velocity looks very similar to Figure 1 of Trott & Webster (2002). Care was taken to align the dark halo’s angular momentum with the azimuthal axis of the disk.

The second galactic system implanted is modeled after a generic elliptical galaxy. To help in interpreting our results, we set the total baryonic mass to be the same as in the early-type spiral system. The elliptical is given a spherical Hernquist profile with effective (half-mass) radius of 7 kpc, and is subsequently deformed into a tri-axial shape with projected ellipticities of 0.03, 0.16 and 0.33 depending on the viewing angle and is aligned with the tri-axial shape of the unperturbed halo.

Each of our two implanted galaxies was realized with 50,000 particles and the total system, baryonic galaxy plus dark matter halo, was run forward in time using the N-body code GADGET (Springel et al., 2001) for 200 Myr. The baryonic particles were held fixed in position while the dark matter halo was allowed to dynamically respond to the imposed galaxy potential. Due to the instantaneously imposed baryonic potential, the dark matter halo becomes more spherical and contracts, increasing its central density. Prior work has suggested that our instantaneous application of the baryonic potential is not much different then slowly growing it within a dark matter halo (Jesseit et al., 2002).

2.1. Ray-Tracing

To study the lensing properties of our simulated galaxies we must determine the deflection angle as a function of position on the sky. It is an excellent approximation in this case to treat the mass as if it were in a single plane – the lens plane. A viewing angle is chosen and the mass distributions is projected to find the surface density, $\Sigma(\vec{x})$. We can then calculate the dimensionless surface density or convergence

$$\kappa(\vec{x}) = \Sigma(\vec{x})/\Sigma_{cr}. \quad (1)$$

The critical surface density is

$$\Sigma_{cr} = \frac{c^2 D_s}{4\pi G D_d D_{ds}}, \quad (2)$$

where D_s is the angular diameter distance between the observer and the source, D_d is the angular distance between the observer and the lensing plane, and D_{ds} the angular distance from lensing plane to source plane. We have chosen to put the source at $z=3.0$ and the lens plane at $z=0.8$, which for a standard Λ CDM concordance model ($\Omega_{\Lambda} = 0.7$, $\Omega_m = 0.3$) with $H_o = 70 \text{ km s}^{-1} \text{ Mpc}^{-1}$ gives $\Sigma_c = 1.92 \times 10^9 M_{\odot}/\text{kpc}^2$.

The surface density can be related to the deflection potential, $\psi(\vec{x})$, through the Poisson equation

$$\nabla^2 \psi(x) = 2\kappa(x), \quad (3)$$

where all derivatives are with respect to distance on the lens plane. The potential is in turn related to the the deflection angle $\vec{\alpha}$ by

$$\vec{\alpha}(x) = \nabla \psi(x), \quad (4)$$

so that the position of the source on the lens plane, \vec{y} , is given by the lens equation: $\vec{y} = \vec{x} - \vec{\alpha}(\vec{x})$. The magnification matrix is $A_{ij} \equiv \frac{\partial y^i}{\partial x^j}$ and the magnification of an infinitesimal image at \vec{x} is $\mu(\vec{x}) = |A|^{-1}$.

We solve the above equations in discrete Fourier space. To estimate the surface density on a regular grid from the simulations’ particle positions we use a Cloud in Cell (CIC) routine (<http://idlastro.gsfc.nasa.gov>). This routine distributes the mass of each particle over the four pixels closest to the particle position. The fraction of the mass in each pixel is weighted by how close the particle lies to the center of the pixel. We use a 4096×4096 grid at this stage.

Solving the equations in Fourier space imposes unphysical periodic boundary conditions. To overcome this problem, we pad our simulations with zeros on the borders. By doing this we effectively separate our galaxies from their mirror images to the extent that they do not affect each others’ strong lensing properties. We find that filling an array of 3052×3052 with our simulated galaxies and filling in the rest of the 4096×4096 grid with zeros gives us the level of accuracy we need in the inner regions where strong lensing occurs.

The deflection angle (4) is calculated at uniform grid points on the lens plane and the lens equation allows us to map each image pixel back to a point on the source plane. Nonetheless, mapping back from the source plane to the image plane is not as simple, since each source position can be mapped to many image positions. To overcome this difficulty, a number of techniques have been developed. In the first we pixelize the source plane and associate image plane pixels with the source plane pixels closest to their position when mapped back to the source plane. Through this method, we are able to generate a list of all image pixels associated with any source plane pixel.

The 4096×4096 grid does not provide enough pixels in the inner regions affected by strong lensing to model lensing properties accurately. Once we have calculated lensing properties such as angular deflections, shear and magnification on the grid, the resolution is increased by extracting the central region of interest in strong lensing and using bilinear interpolation to calculate these quantities to higher resolution. This is justified because the numerical resolution of the simulations is already 30% larger than the 4096×4096 grid resolution. Therefore any structure on a smaller scale would be purely numerical noise in any case.

The critical curves on the image plane are where the magnification diverges to infinity. Close images will always be separated by one of these curves. Images on opposite sides of a critical curves have different parities – their magnifications, defined as $1/\det[A]$, have opposing signs. We calculate the magnification at each image pixel and use this fact to separate images that are close to critical curves. In addition, mapping these critical lines back to the source plane with the lens equation allows us to map out the caustic curves – the curves on the source plane where the magnification diverges. The caustic curves also separate regions on the source plane with different image multiplicities.

Using the sign of $\det[A(x)]$ to separate images works well for much of our work, but we found that for small sources near a caustic this methods requires very high grid resolution and becomes too computer intensive. For these circumstances we developed an adaptive mesh technique, which allowed us to study source sizes well below the resolution of the grid on which the lensing equations are solved. We start by find the source position of each grid point on the image plane and calculate its distance from the center of the source. The images are located by finding minima the this distance on the image plane grid. Then higher resolution grids are constructed around these images and the process is repeated. This allows us to cover the three orders of magnitude in length scale required for some of the results that discuss later.

Once the images have been identified we investigated three methods for measuring the magnifications of the images. The most straightforward method is to take the ratio of image size to the source size by counting the number of pixels in each image. A second method is to take the average of the inverse of the magnification calculated at each pixel on the image plane that is in the image. The inverse of this is an estimate of the magnification. In the third method, the image of the boundary of the source is found by interpolation. The area on the image plane enclosed in this curve is then calculated by integrating $\vec{r} \times d\vec{r}/d\theta$ around the curve. We find that for isolated images, where none of the images come in contact with the critical curves all methods agree well with each other. However, as the images grow and start to come into contact with the critical curves, the first method becomes less accurate because of the limited grid resolution and the extreme elongation of the images. We also found that, in extreme cases, the results of the boundary method can be dependent on the interpolation algorithm used. For these reason we chose to use the averaging method in all our reported calculations.

3. Results

3.1. Noise Properties with a Singular Isothermal Ellipsoid (SIE)

Because of the finite size of the particles in the simulations there is a significant amount of shot noise in the surface density estimate which in turn affects the lensing properties. We will remove this noise by smoothing the surface density with a Gaussian kernel, but first we need to calibrate the process by applying it to a case where the lensing properties are already well known. To do this, we add noise to a simple SIE lens model and repeatedly smooth it to find the minimum smoothing length that reproduces the expected image magnifications with sufficient accuracy.

First, we calculate the surface density of a SIE with caustic features similar to those seen in our simulated halo (figure 2). We then create two different realizations with the level of shot noise we would expect if the SIE is made up of the same number of particles as our simulated halo. The shot noise is reproduced by first producing an array of normally distributed random numbers and then convolving it with a two dimensional kernel designed so that the second order correlations between the pixels are the same as those expected in the CIC estimate of the surface density with Poisson fluctuations in the particle numbers. Since the particle density is high in all the regions of interest here we expect that the central limit theorem holds and the noise will be close to Gaussian. There is no guarantee that the Poisson assumption will give an accurate estimate for the magnitude of the shot noise. As will be commented on later, when a random realization of this noise is added to a real simulation the surface density tends to get less smooth and the lensing properties more irregular. For this reason we suspect that this is an overestimate of the noise.

We first look at the effects on critical curves and caustic structure. We find that the addition of shot noise does not significantly alter the shape of the caustics, but it does seem to affect the outer (tangential) critical curve. We see the same thing in section 3.2. This outer critical curve is close to the $\kappa = 0.5$ contour which is a region of much lower density than the inner (radial) critical curve. This may explain the outer critical curve's higher sensitivity to shot noise, which can also be seen in Figure 3. Since the magnification becomes very large near the caustic curves, the variations in outer critical curve could have significant effects on image magnifications (further examined in sections 3.3 and 3.4). We investigate this by choosing one

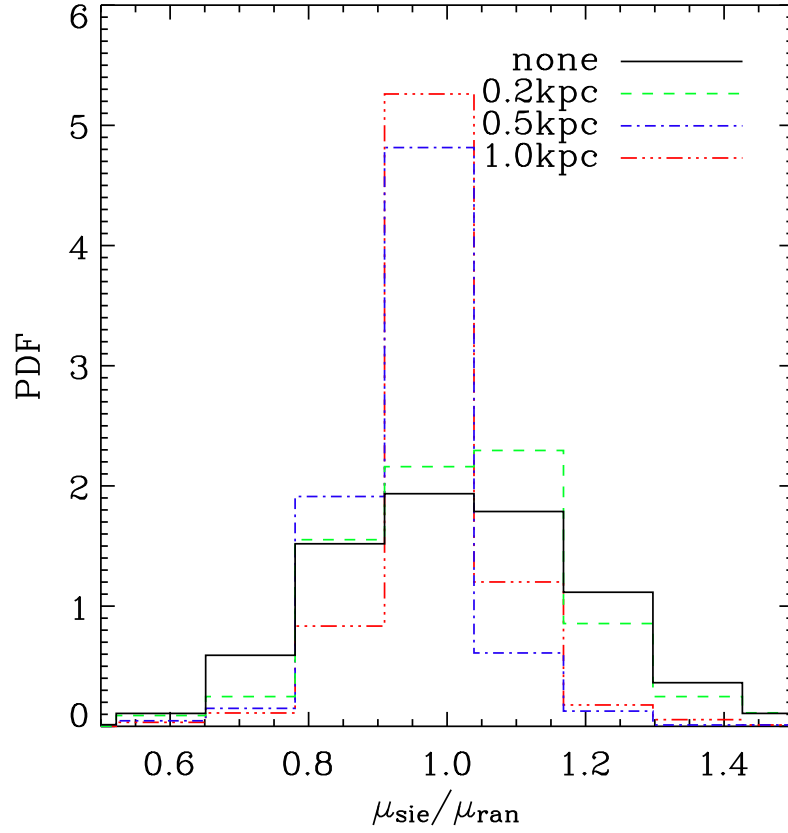


Fig. 1.— The Probably Distribution Function (PDF) for the ratio of the magnifications of images formed in the Singular Isothermal Ellipsoid relative to the corresponding images in the realization with random noise. We see that without smoothing (solid black), the random shot noise introduces a large spread in magnification. The histograms are labeled with the width (2σ) of the Gaussian used to smooth the surface density. We see that smoothing with a width of 0.2 kpc or below does not have a significant effect. To reduce the effect of noise to a sufficient level we need to use a smoothing scale of 0.5 kpc. The standard deviations of the PDF's with no smoothing, 0.2 kpc, 0.5 kpc and 1.0 kpc are $\sigma = 0.23, 0.21, 0.12$ and 0.12 .

Case	2 images	4 images	3 images
S edge on	0.54	0.34	0.113
S face on	0.95	0.05	0.000
S 30° spiral	0.79	0.21	0.003
S mean of 50	0.66	0.27	0.064
E orientation 1	0.92	0.08	0.000
E orientation 2	0.88	0.12	0.000
E mean of 50	0.93	0.07	0.000

Table 1: Table showing the relative sizes of the the 2 image, 4 images and 3 image regions of the lens. For the disk case we show the results for three orientations as well the mean over 50 random projections. For the elliptical galaxy we show two orientations as well as the mean over 50 random orientations.

hundred random source positions that lie within the caustics. For each of these positions we calculate the positions and magnifications of the images formed in each realization and compare the magnifications to the SIE model. Significant discrepancies are seen before smoothing. We smooth each of the three SIE realizations with a Gaussian kernel of widths (2σ) of 0.2, 0.5 and 1.0 kpc giving a total of 12 realizations (including the original SIE’s without smoothing). For each smoothing scale we study the variation in magnification of the images formed from the one hundred source positions. The results are shown in Figure 1. With a smoothing scale of 0.5 kpc, the magnification has a standard deviation (σ) of 0.12, which we judge to be small enough for our investigations and we adopt it in later sections. This is also the smoothing scale for the N-Body code used to construct the dark matter halo. Therefore, we can use this level of smoothing without losing any real spacial information. It should be noted however that the same amount of smoothing will not result in the same variance in the magnification ratios for every source location. For some source locations the magnifications could be more or less sensitive to shot noise.

3.2. Caustic Structure & Image Multiplicities

Here we show the caustic structures, critical curves and convergence maps for a number of viewing angles through our disk galaxy. In Figure 2 shows the case of our disk galaxy inclined at an angle of 30 degrees to the line of sight. The result of smoothing the surface density is shown in Figure 3. We find that the noise does affect the outer critical curve, which is the image of the inner (tangential) caustic curve. Noise has the greatest effect close to the cusps in the caustic, where we see some ‘dove tail’ structure as seen by Bradač et al. (2003). However, we do not see as many of these features as they do. This could be because their simulated lens is much more concentrated and the density at the critical curve is lower which increases the shot noise and because their particle mass is larger.

In Figure 4, we see the convergence, critical curves and caustics for two cases: one with the disk face on to the line of sight and the second with the disk edge on to the line of sight. In these images we see a large variation in the the area of the two-image regions and the four-image regions (not counting the central demagnified image). In the edge-on case, we also see the cusps of the tangential caustic extending out beyond the radial caustic, forming what is called a *naked caustic*. If the source is in this region, three observable images and no central image are

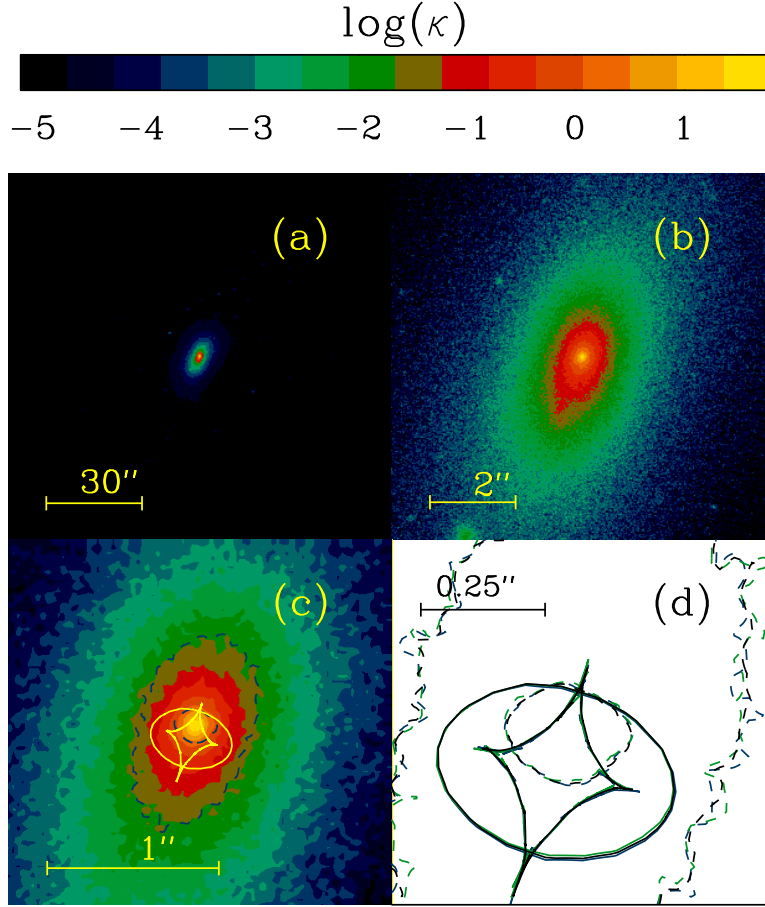


Fig. 2.— The simulated galaxy with the disk inclined at a 30 degree angle to the line of sight. Figure (a) shows the surface density of the entire galaxy along with the buffering we use to make sure the repeating boundary conditions do not affect our results. In (b) we see the inner region that is of interest to us. Here there is some substructure which affects some of the overall lensing, properties such as the offset of caustics to density peaks as seen in (c). In (c) the critical curves are shown as dashed curves and the caustic curves are shown in yellow. The critical curves clearly have small scale irregularities. In (d) we look at the inner caustics region and how it is affected by random noise. Results for three realizations of the shot-noise are shown in black, green and blue. Without smoothing, shot-noise does affect the critical curves, which, in turn are mapped back to the caustics. We see some evidence for dove tail features in the caustics, but they are not prominent and the inner (radial) caustic is relatively stable. No smoothing of the surface density has been done here. In the inner regions, where multiple images form, roughly 2/3 of the surface density is due to dark matter where as the remaining 1/3 is due to baryons

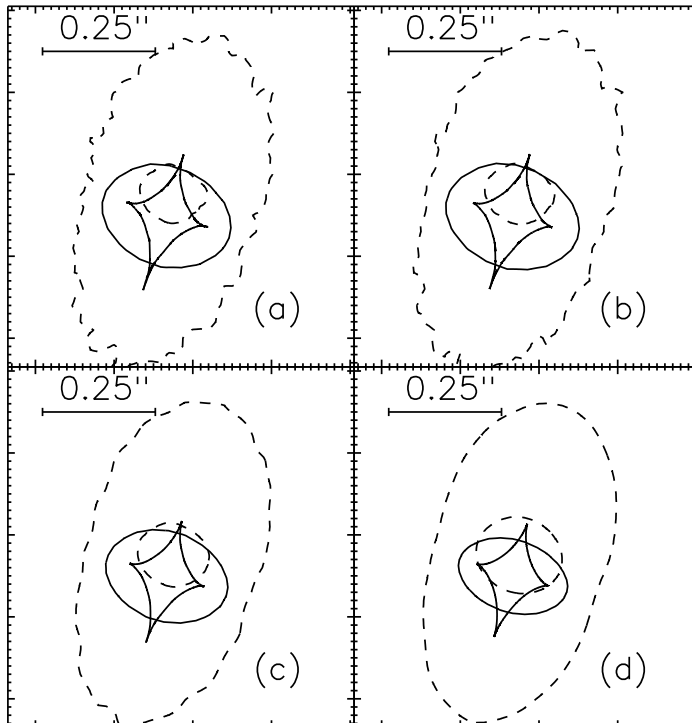


Fig. 3.— The effects of smoothing on caustic critical curve structure. Panel (a) shows the results with no smoothing. Panels (b), (c) and (d) show the caustic structure and critical curves with Gaussian smoothing on scales 0.2, 0.5 1.0 kpc, respectively. We see that the general shape of the outer critical curves (and hence the star caustic which corresponds to it) is largely unaffected by the smoothing. The smoothing, however, does affect small scale variations of these lines, making them more smooth. The radial (inner) critical curve (and the corresponding oval caustic curve) is affected in exactly the opposite way. On small scales, the noise and smoothing do not affect the curves. This is because the regions close to the inner critical curves have a high density, hence they are less sensitive to shot noise. The Gaussian smoothing, however, does cause the inner critical curve to expand and the oval caustic region to shrink. This is because smoothing flattens the inner cusp region of the galaxy.

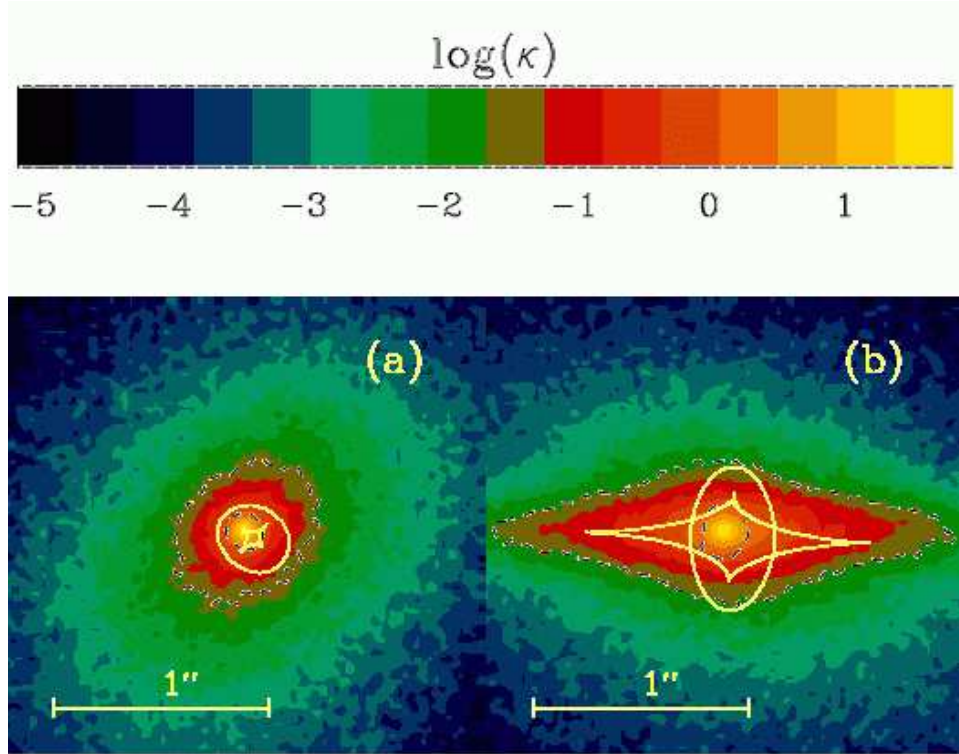


Fig. 4.— On the left, (a), is the surface density, critical curves and caustics for the face on disk and on the right, (b), is the same quantities for the edge on disk. Between these two extreme cases we can see distinct changes in the caustic features. In the face on case, where the surface density is almost circularly symmetric the inner, four image, caustic is small. In the edge on case, one effect of the disk is to extend the inner caustic. This inner caustic is so enlarged that we see large naked caustic regions – regions where the inner caustic extends out beyond the outer caustic and three images are observable.

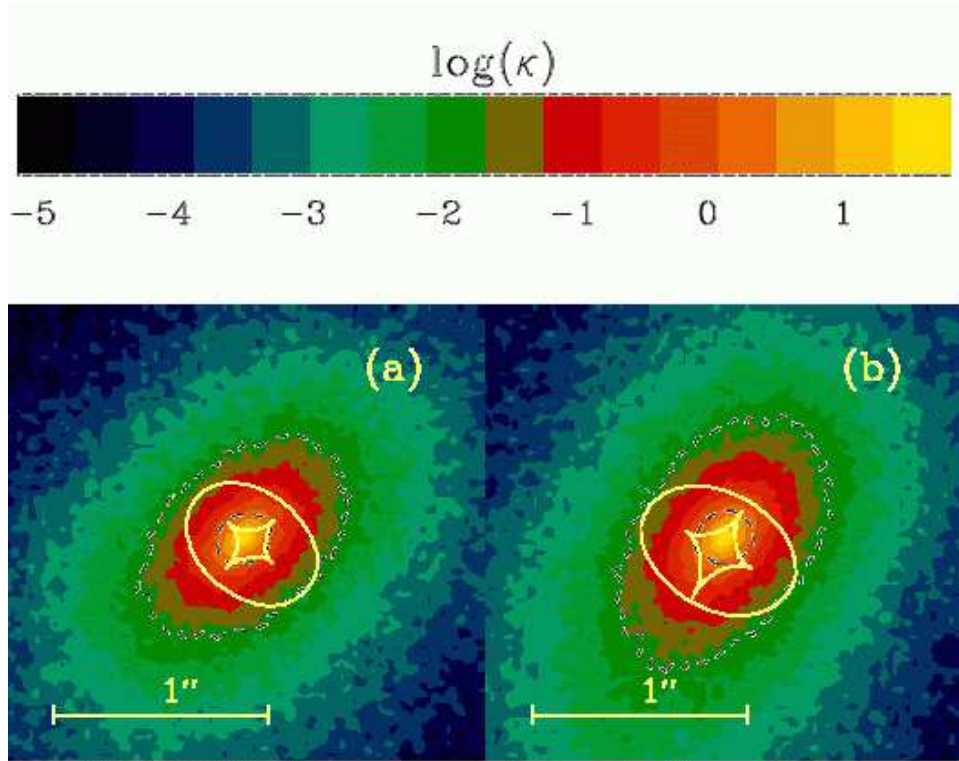


Fig. 5.— The surface density, critical curves and caustics for two orientations of the elliptical galaxy - a) orientation 1 and b) orientation 2 as in table 1. We see that the elliptical galaxy does not show the large extended inner caustic that we see for the disk case. This shows that the elliptical surface densities are more circularly symmetric, thus making it very difficult to create three image systems.

formed. To determine the relative numbers of four image to two image systems as well as the abundance of naked caustics, we measure the area of the caustic regions in several orientations. We also do the same measurements for 50 random projections of the galaxy, and separate the caustic regions into three subregions. The first (four images) is region that falling inside both the tangential and radial caustic. The second (two images) is the region falling inside the radial caustic and outside the inner tangential caustic and the final region (three image) is inside the tangential caustic and outside the radial caustic.

The relative areas of these regions and thus the fractions of expected lens configurations are reported in table 1. The observed ratio between the number of four to two image lenses is $\sim 50\%$ in the JVAS/CLASS surveys (Myers et al., 2003), much larger than what is seen here. Since most lenses do not contain disk galaxies the discrepancy is particularly striking. Our simulations do not constitute a statistically significant sample, but the discrepancy is still uncomfortably large. Magnification selection bias, which depends on specific observational selection criteria of a survey, is an important factor that may go some way towards explaining the discrepancy. In future, with a larger more statistically significant sample, the extent of magnification bias can studied in more detail. It could also be that companion or satellite galaxies play a role in increasing the four image fraction as proposed by Cohn & Kochanek (2004), but any companions within 265 kpc should be included in our simulations.

In Figure 2, we see that the caustics are not centred on the density peak. This is due to the lack of symmetry in the surface density and in particular to the presence of a substructure just below the density peak visible in Figure 2, Panel b. We also look at this offset in our 50 random realizations and find a mean offset of 0.08 arc-seconds.

3.3. Differential Magnification Ratios

Modeling lenses in search of substructure has proven to be difficult due to degeneracies in the lens models. Metcalf et al. (2004) used the technique of spectroscopic gravitational lensing to overcome some of these degeneracies. This technique relies on the assumption that without substructure the magnification ratios will be independent of the source size (for sizes $\lesssim 1$ kpc). In this section, we seek to test this assumption for our simulated lenses in different image configurations and thus determine whether a mismatch in the magnification ratios at different wavelengths can be considered strong evidence for the presence of substructure.

Our simulated halo has a resolution of $1.68 \times 10^6 M_\odot$ so it will not have any substructures less massive than a $\sim 8 \times 10^7 M_\odot$, which is at the very limit of the mass range for the substructure found in Metcalf et al. (2004). For this reason we do not expect to be able to represent the kind of structure that could be responsible for those results, but we can verify the assumption that larger scale irregularities in the lens will not cause mismatches in the ratios at different wavelengths.

We look at the sensitivity of the magnification ratios to source size in three types of image configurations. First, the Einstein cross configuration shown in figure 6 which has four relatively symmetrically spaced images. The second configuration comes from placing the source close to a cusp in the caustic. This produces three images that form close together and one isolated image. By placing a source close to each of the four cusps we produce four versions of this configurations, shown on the left in figure 7. Thirdly, we place the source near a fold caustic forming a pair of closely spaced images with a further two images that are more widely spaced. Again, by placing a source near each fold, we have four realizations of this fold caustic configuration (shown on

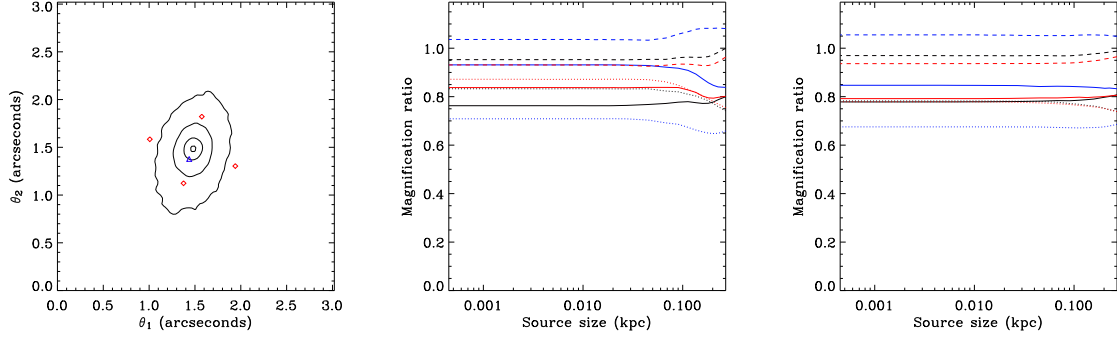


Fig. 6.— On the left is the image configuration for an Einstein cross formed when the source is near the center of the radial caustic for the disk galaxy case inclined at 30° . The four bright images (red diamonds) correspond to the source position indicated by the blue triangle. The contours show the surface density (with Gaussian smoothing = 0.5 kpc), the levels are $\kappa = 0.5, 1.0, 2.0$ and 4.0 . The two panels on the right show magnification ratios as a function of source size. The middle panel shows results *without smoothing* and the right panel shows the ratios when the surface density smoothed with a Gaussian kernel of width $2\sigma = 0.5$ kpc. The solid curves show the magnification ratios of the closest image pair, the dotted curve shows the magnification ratio of the other two images, and the dashed curves shows the ratio of the average of each pair (see discussion in § 3.3). The black lines are calculated using the n-body simulations where as the red and blue lines are calculated after two realizations of the estimated noise has been added.

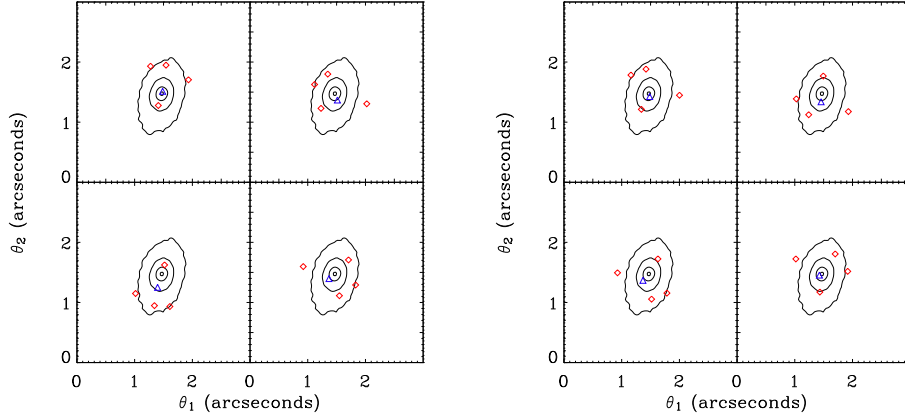


Fig. 7.— The image configurations used to test the dependence of the magnification ratios on source size. On the left are four configurations with the source close to a cusp in the caustic and on the right are four configurations with the source close to a fold caustic. As in figure 6 red diamonds mark the images and blue triangles mark the source position. The contours are as in figure 6

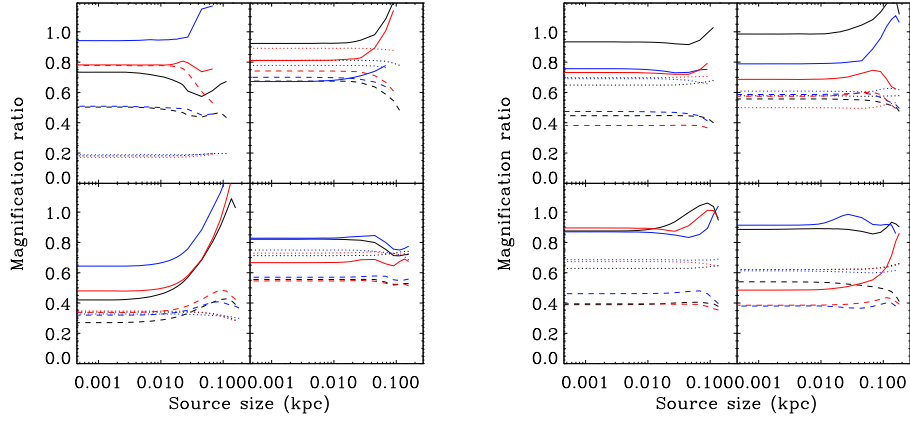


Fig. 8.— The magnification ratios of the the four bright images as a function of source size for the realization of the inclined disk (30°) *without smoothing*. The solid curve shows the magnification ratios of the close image image pair, the dotted curve shows the the magnification ratio of the other two images, and the dashed curves shows the ratio of the average of each pair. Shown here are the results of ray tracing through the original simulated galaxy and halo (black) and the results from simulations with random noise (blue and red) without smoothing. The cusp configurations are shown on the left and the fold configurations on the right, in the same order as in figure 7. Much of the variations in the ratios seen here are caused by shot noise as can be seen by comparing this figure to figure 9 where the shot noise has been removed by smoothing. Also note that it is the solid curves that show the largest dependence on source size.

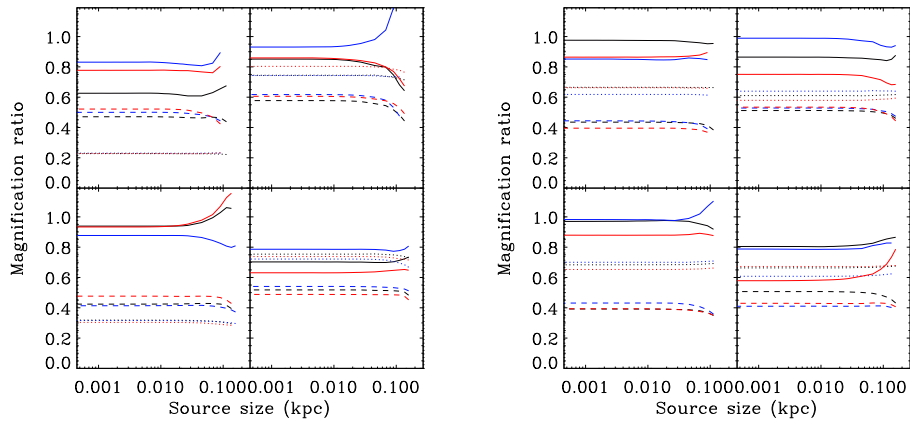


Fig. 9.— The same quantities as in figure 8, but with the simulated galaxy/halo smoothed with a Gaussian kernel of width $2\sigma = 0.5$ kpc. The variations in the magnification ratios as a function of source size are significantly smaller than in figure 8 where no smoothing was applied. The variations are largely isolated to the ratio for the closest pair of images (solid curves).

the right of figure 7).

Figure 6 shows the results for an Einstein cross configuration with the disk galaxy inclined at 30° . Based on the assumptions made in Metcalf et al. (2004) we would not expect to see any significant variation in magnification ratio in this case and there are none seen. The magnification ratios being a strong function of source size is a strong indication that there are structures smaller than the ones represented in these simulations.

Figure 8 shows the cusp and fold caustic results with no smoothing and Figure 9 shows the results for the surface densities smoothed with a Gaussian of width $2\sigma = 0.5$ kpc. A potential complication with the interpretation of the differential magnification ratios is that when the source is large it could overflow the radial caustic region, especially in cusp and fold caustic configurations. In this case, part of the source has four images and part of it has two images. This potential problem can be reduced by a judicious choice of magnification ratios. The closest two images are usually images of only the part of the source that is inside the tangential caustic. The other two images are of all parts of the source that are within the radial caustic, usually a superset of the former region. In theory, the magnification ratios of this image pair should be the least sensitive to source size – at least when the source is large. We single out these ratios in the figures. For the third ratio, we choose to use the ratio of the average flux from each pair. This ratio is potentially affected by the source’s “overflow” of the tangential caustic region.

For both the fold and cusp caustic cases, with smoothing (figure 9), we find that the magnification ratios are insensitive to sources size while the size is below several hundred pc. Any variation there are mostly isolated in the ratio between the closest pair of images. In general, the further images are separated the less their magnification ratio will depend on source size. This is consistent with what we had expected – that the images close to the critical curves, which have high magnifications, will respond to small variations in the critical curves introduced by substructure (Figure 2d). The ratios for the wide separation pairs (dotted curves in figure 9) are effectively independent of source size and thus a large observed dependence can be considered a trustworthy indicators of smaller scale substructure or some other complicating effect.

We also see, by comparing figures 8 and 9, that the shot noise, or more generally smaller scale structure, has a significant effect on the magnification ratios (figure 8), but the generic feature that the ratios are stable for sizes below 10 pc is preserved in all cases and the variation that are there are largely isolated to the most closely spaced image pair. It is also evident from figures 6 through 9 that the values of the magnification ratios are dependent on the realization of the shot noise. We interpret this as the influence of changes in the surface density that are too large in scale to produce a variation with source size, but still significant enough to change the magnification ratios.

3.4. The Cusp Caustic Relation

Evidence that the cusp caustic relation is violated may provide a way of probing the abundance and nature of substructure in lensing galaxies and/or small scale structure in intergalactic space. All the observed cusp caustic lenses violate this relation at some level (Mao & Schneider, 1998; Keeton et al., 2003). In order to understand the significance of such results, it is important to study the ways in which this relation is affected by structures in the lensing galaxy. Keeton et al. (2003) has studied the cusp caustic relation in a wide range of smooth analytic lens models and Bradač et al. (2003) have looked at the relation in simulations. In this

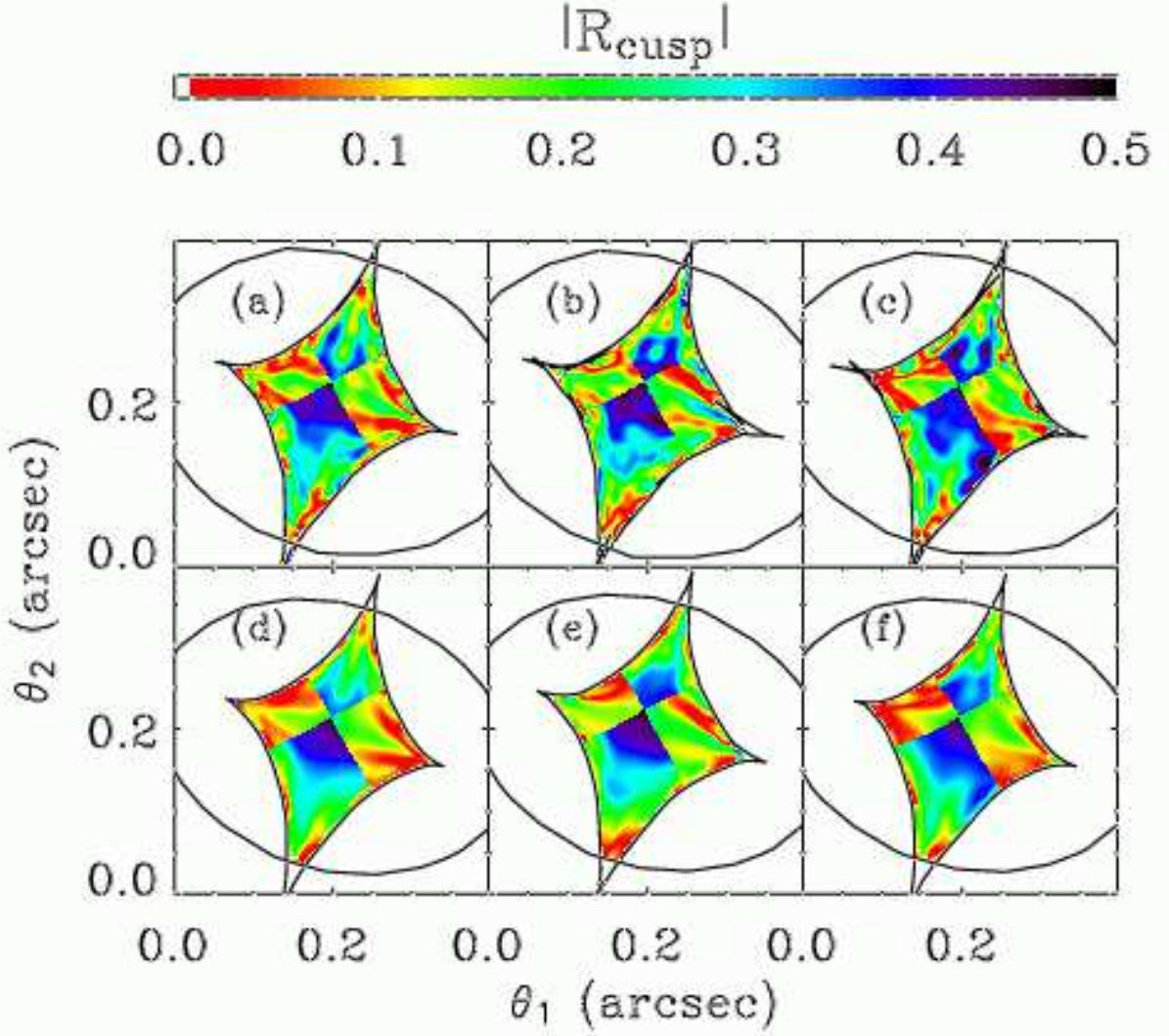


Fig. 10.— Value of the quantity R_{cusp} across the four image region of the source plane for each realization of the noise using a 60pc source. Panel (a) shows the results for our inclined disk realization, (b) and (c) show the same quantities with the addition of random shot noise. Panels (d), (e) and (f) show the corresponding results when the surface density is smoothed with a Gaussian of width 0.5 kpc. The discontinuous jumps are where the three closest images change. Not all the regions near the cusps are red as would be expected from the cusp caustic relation. There are “dove tails” in the caustics that appear to be associated with significant violations in the relation.

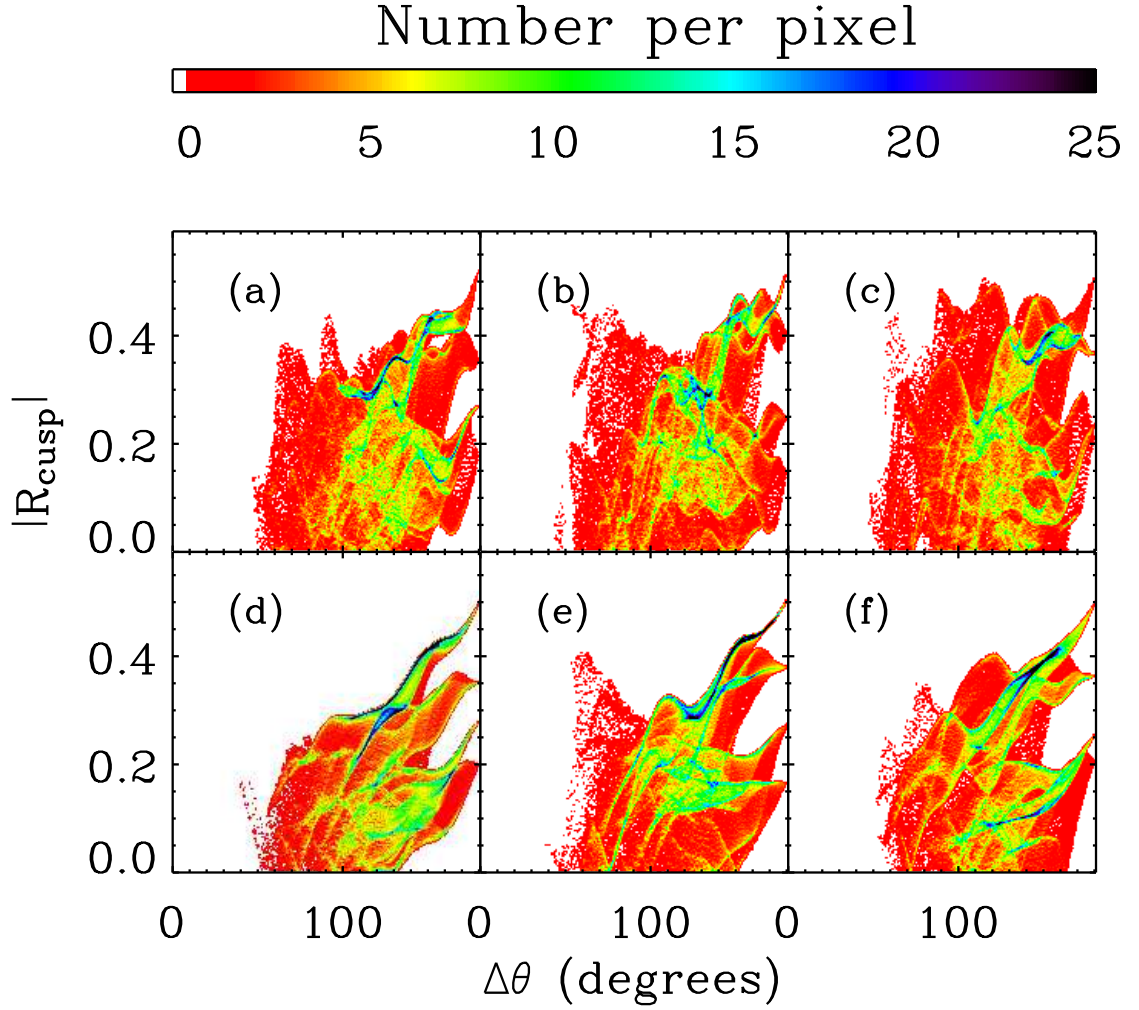


Fig. 11.— Variation in R_{cusp} as a function of the angular separation $\Delta\theta$ of the closest three images. The results here are for a source with a radius of 60pc. Panel (a) shows the results for our inclined disk realization, (b) and (c) show the same quantities with the addition of random shot noise as in figure 10. Panels (d), (e) and (f) show the corresponding results when the surface density is smoothed with a Gaussian of width 0.5 kpc. The color coding is explained in the text.

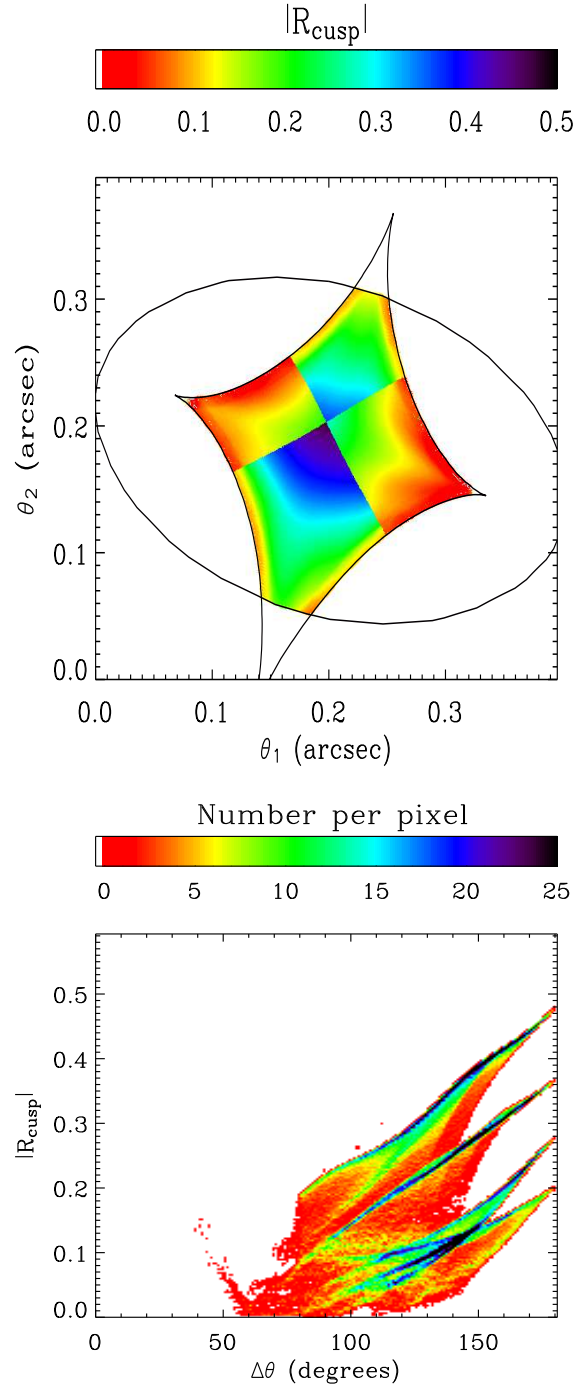


Fig. 12.— The same as figures 10 and 11 except with a smoothing length of $2\sigma = 1.0$ kpc. No random noise has been added. The tangential caustic has expanded because the smoothing has reduced the concentration of the halo.

section, we examine violations of the cusp caustic relation for our simulated galaxy+halos and attempting to establish the number of violations that should be expect in Λ CDM.

We study the cusp caustic relation by placing a source inside both the radial and tangential caustics. Source positions in this region produce 5 images, with the fifth image begin close to the center of the lens. For the work in the section we discard this central image from the analysis routines since it is usually hard to identify due to its demagnification. The remaining four images consist of two images with positive parity and two images with negative parity.

Identifying the images of extended sources is often difficult when their magnifications are high, as they are in cusp caustic configurations. The images can be drastically stretched and curved near the outer (tangential) critical curve. In such a situation, a single image can be identified as two or more separate images because of limited grid resolution. In this study we decided to "err on the side of caution" and have included only the results for source positions where we find four outer images with a total parity of zero (+,+,-,-). As in the previous section, we have performed consistency checks on the calculated magnifications with multiple methods. We find that both of these independent methods give consistent results.

For each of the lenses studied, the region of the source plane which produces four images is divided into a two dimensional grid with a grid spacing of 10 pc. This gives us roughly 70,000 source position to study. We place one sources of radius 60 pc at each grip point, producing the four images. We then identify the three closest images, which we define as the three images that subtend the smallest azimuthal angle using the peak of the surface density as the center of the co-ordinate system, denoted $\Delta\theta$. These images allow us to measure the cusp caustic parameter,

$$R_{\text{cusp}} = \frac{\mu_1 + \mu_2 + \mu_3}{|\mu_1| + |\mu_2| + |\mu_3|}. \quad (5)$$

We also check that the middle image of the three has the opposite parity to the other two images. This process is repeated for all the grid points.

The cusp caustic relation states that as the three images move close together the quantity R_{cusp} should tend to zero (Schneider & Weiss, 1992; Zakharov, 1995; Keeton et al., 2003). Figure 10 shows our results, with panel (a) showing our calculations using the disk galaxy inclined at 30° and panels (b) and (c) showing the results for the inclined disk with the addition of shot noise. Panels (d), (e) and (f) show results corresponding to the same realizations as (a), (b) and (c), but smoothed with a Gaussian kernel of width $2\sigma = 0.5\text{kpc}$. Figure 12 shows the same simulation with a smoothing length of $2\sigma = 1.0\text{ kpc}$.

We see a similar variation in R_{cusp} over the source plane as seen by Bradač et al. (2003) in their elliptical galaxy simulation, but less variation than in their disk galaxy simulation. This could be because of their larger particle masses. Shot noise does seem to have a larger influence on their results. Without smoothing, shot noise has significant effect on the features in our R_{cusp} map. This is not surprising since, as we have already discussed, images with high magnification (close to the critical curves) are most susceptible to shot noise. Gaussian smoothing has the expected result of reducing the variation of R_{cusp} over the caustic, as well as reducing the discrepancy between the realizations with and without the addition of shot noise. Figure 12 shows that when the simulation is over-smoothed a regular and expected pattern in R_{cusp} emerges. Despite this, there are still significant regions near the cusps in the $2\sigma = 0.5\text{ kpc}$ simulation where R_{cusp} is not small. The importance of these regions needs to be quantified.

Figure 10 also shows that when the cusp in the tangential caustic is near the radial caustic, R_{cusp} is not particularly small. This brings up the possibility that violations in the cusp caustic

	No smoothing	$2\sigma = 0.5$ kpc	$2\sigma = 1.0$ kpc
S 30° spiral	0.26	0.10	0.00
S random 1	0.22	0.13	-
S random 2	0.28	0.13	-

Table 2: The ratio of points in figures 11 that violate the cusp caustic relationship ($|R_{\text{cusp}}| > \Delta\theta/360^\circ$) to the total number of data points.

relation might be the result of such near-naked cusp caustic cases. Such cases will only occur when the source is near a cusp pointing in the direction of the lens’s long-axis. These cases can be distinguished from short-axis cusp caustic cases by the position of the fourth image – it tends to be close to the center of the lens for long-axis cases and well outside the radial critical curve (the Einstein radius) for short-axis cases. For this reason the cusp caustic relation might be considered more trustworthy for short-axis cusp caustic lenses.

Figures 11 shows $|R_{\text{cusp}}|$ as a function of the angular separation of the closest three images. The $|R_{\text{cusp}}|, \Delta\theta$ plane is divided up into a 200×200 grid forming pixels of $0.9^\circ \times 0.003$. The color scale shows the number of results that fall in a given pixel and so the figure can be thought of as a 2D histogram – more likely combinations are green or blue and the less likely red. Panels a, b, and c show a great deal of scatter. Figure 12 shows the same type of plot only with the surface density smoothed with $2\sigma = 1.0$ kpc. It is clearly necessary to define what is meant by a violation of the cusp caustic relation since we would clearly not expect R_{cusp} to be precisely zero even without substructure. For this we draw a line from $[\Delta\theta, |R_{\text{cusp}}|] = [0^\circ, 0]$ to $[180^\circ, 0.5]$ and call all the point above this line, i.e. $|R_{\text{cusp}}| > \Delta\theta/360^\circ$, a violation. This definition is chosen so that there will be no violations in the over-smoothed case.

This is a very crude definition and it is possible to make a more restrictive one by incorporating more information about individual lenses. We will error on the side of not identifying all the cases that are true anomalies. Table 2 shows the fraction of cases where the relation is violated by this definition. The fractions are significant but not large. Table 2 and figure 11 bring up the issue of how well we have estimated the shot noise in the simulations. It is clear that in the cases where we added noise there are more violations of the cusp caustic relation and figure 10 looks less smooth. It is very possible that we overestimated the noise. If this is true, the case in table 2 with no noise added should be the best estimates for the fraction of violations, $\sim 10\%$.

There is an interesting underlying pattern on the $R_{\text{cusp}}\text{-}\Delta\theta$ plane. This pattern becomes more defined and clear with increased smoothing, becoming clearest in figure 12. R_{cusp} is restricted to 4 discrete values when $\Delta\theta \sim 180^\circ$, each corresponding to the different quadrants of the star caustic. This is not surprising since $\Delta\theta = 180^\circ$ corresponds to one point on the source plane.

3.5. A Very Brief Comparison With Observations

Properties of the observed cusp caustic lenses are summarized in table 3. The observed number of violations, by the criterion used in this paper, is 3 out of 5. This is significantly larger than the 10 – 13% we found for our simulations in section 3.4. Keeton et al. (2003) have

lens	$\Delta\theta$	R_{cusp}	observed band	cusp caustic violation?
B0712+472	79.8°	$0.26 \pm 0.02^{1,2}$	radio	yes
B2045+265	35.3°	0.501 ± 0.035^2	radio	yes
B1422+231	74.9°	$0.187 \pm 0.006^{2,3}$	radio	no
RXJ1131-1231	69.0°	0.355 ± 0.015^4	optical/IR	yes
RXJ0911+0551	69.6°	0.192 ± 0.011^5	optical/IR	no

Table 3: The image opening angles and cusp caustic parameters for the observed cusp caustic lenses. The criterion on which it is judged to violate the cusp caustic relation is if $R_{\text{cusp}} > \Delta\theta/360^\circ$. RXJ0911+0551 is right on the border of this cut.

¹Jackson et al. (1998)

²Koopmans et al. (2003)

³Patnaik & Narasimha (2001)

⁴Sluse et al. (2003)

⁵Keeton et al. (2003) & the CASTLES survey

considered these same lenses and concluded that all but B1422+231 violate the relation by a different definition. The numbers are still clearly very small, but the disagreement is large. This is an indication that at least the substructure that is resolved in these simulations is not enough to cause the observed anomalies.

Interestingly, all the lenses in table 3 except RXJ0911+0551 are long-axis cusp caustic lenses. These are the type in which the cusp in the tangential caustic can potentially come close to the radial caustic where the cusp caustic relation might not be valid. This only occurs when lens is sufficiently non-axisymmetric. This is the case for the simulated lens we used in section 3.4 so in a crude way this possibility is taken into account. In any case, as was shown in section 3.2, this is not likely to happen for an elliptical galaxy and most lenses are ellipticals. Because they are elliptical we should really expect even fewer violations than 10 – 13%.

The results of section 3.3 show that the assumption of spectroscopic gravitational lensing are sound. The discrepancy between the radio, mid-infrared and narrow line magnification ratios of Q2237+0305 (Metcalf et al., 2004) can not be accounted for by Λ CDM halos because there are too few with masses $\lesssim 10^7 M_\odot$. This result has yet to be confirmed with other lenses or adequately explained.

4. Conclusions & Discussion

Galactic sized gravitational lenses have been simulated by combining a cosmological N-body simulation with models for the baryonic component. The lensing properties have been calculated through a combination of ray-shooting and adaptive mesh refinement with the goal of study the effects of the substructure.

The main conclusions are: (1) The image magnifications in the Einstein cross configuration are very weak functions of source size when it is below ~ 1 kpc. In the fold and cusp caustic cases we find the same thing for the magnification ratios of widely separated images. This confirms the belief that spectroscopic gravitational lensing can be used to detect small scale

structure (Moustakas & Metcalf, 2003; Metcalf et al., 2004). (2) If there is no substructures below ~ 0.5 kpc we expect that the cusp caustic relation (by the definition $R_{\text{cusp}} < \Delta\theta/365^\circ$) would hold for $\sim 90\%$ of the lenses. Only 2 of the five observed cusp caustic lenses satisfy this requirement. (3) The ratio of four image lenses to two image lenses in our simulations appears low in comparison to observations. This could be a chance artifact from using too few simulations or it could indicate that some other explanation is required.

It might be that all the halo substructure produced in the Λ CDM is not enough to account for the cusp caustic violations. The amount of substructure in the simulations used here ($\gtrsim 8 \times 10^7 M_\odot$) is not enough and there is not expected to be much more mass in compact enough substructures below our resolution. This argument was made by Mao et al. (2004) and depends on how much substructure is destroyed in the inner regions of the lens halo. It should be possible to see explicitly if smaller scale substructures contribute to the lensing using future simulations and the techniques developed here. Metcalf (2004) recently argued that the observed cusp caustic anomalies can be accounted for by intergalactic halos within the Λ CDM model. Distinguishing between these contributions will be important.

We have tried to estimate the uncertainties in the lensing properties caused by the limited resolution of the simulation by introducing random realizations of the estimated noise to the surface density. It appears that we may have overestimated of the actual shot noise in the simulations, because the simulations with noise added tend to have more irregular critical curves and R_{cusp} distributions than the original simulation. This makes our estimates of the uncertainties in the lensing properties more conservative. Bradač et al. (2003) in a similar study estimated the noise by displacing individual particles at random. Shot noise had a larger affect on their simulations probably because of their larger particle masses. We do not see as many dove tail caustics and violations of the cusp caustic relation as Bradač et al. (2003) did. We think that this is because of their limited resolution and the different radial profile of their lenses.

We have used only one simulated dark matter halo in this study so small number statistics could be an issue in interpreting the results. It could be that a bias has been introduced because the simulated dark matter halo used here was preselected to be relatively isolated and dynamically relaxed. A random sample of halos might have more irregular structure with remnants of recent mergers in them. This could produce more anomalous lensing behavior than is seen here. For example, there is a prominent substructure in the halo that is within $2''$ of the center of the galaxy in the projection shown in figure 2. There could be several of these in a less relaxed halo.

The limiting factor in this study has been the resolution of the cosmological simulation. Because of the limited force and mass resolution, we expect that the central cores of substructure may be destroyed. It is interesting to note that lensing through the realisations without smoothing leads to 30% of cases violating the cusp caustic relation, which is not enough to be in agreement with observations. Since these unsmoothed cases contain close to the maximum granularity in the mass range 10^4 to $10^7 M_\odot$, this indicates that the discrepancy between observation and prediction may not be solved simply by performing higher resolution simulations. Also the discrepancy is not likely due to insufficient substructure in the dark matter component since the simulations with maximal (though inadvertent) substructure the discrepancy remains. This suggests that the other factors mentioned above, including lensing by structure outside the halo, merger remnants and selection bias, do play a significant role in causing the observed violations of the cusp caustic relation. A collection of higher resolution

simulations have already been done and the next generation of cosmological N-body simulations should resolve substructure up to 2 orders of magnitude lower. This kind of study with improved resolution will allow us to test the significance of each of the dominant factors. With this we will be able to conclusively compare the lensing data with the predictions of Λ CDM.

We thank B. Moore for providing us with the simulated halo. AA also thanks T. Saini and L. King for helpful discussions. Support for this work was provided by NASA through Hubble Fellowship grant HF-01154.01-A awarded by the Space Telescope Science Institute, which is operated by the Association of Universities for Research in Astronomy, Inc., for NASA, under contract NAS 5-26555

References

- Abadi, M. G., Navarro, J. F., Steinmetz, M., & Eke, V. R. 2003, *ApJ*, 591, 499
- Bradač, M., Schneider, P., Lombardi, M., Steinmetz, M., Koopmans, L., & Navarro, J. 2003, preprint, astro-ph/0306238
- Chiba, M. 2002, *ApJ*, 565, 17
- Cohn, J. & Kochanek, C. 2004, preprint, astro-ph/0306171
- Dalal, N. & Kochanek, C. S. 2002, *ApJ*, 572, 25
- Hernquist, L. 1990, *ApJ*, 356, 359
- Jackson, N., Nair, S., Browne, I. W. A., Wilkinson, P. N., Muxlow, T. W. B., de Bruyn, A. G., Koopmans, L., Bremer, M., Snellen, I., Miley, G. K., Schilizzi, R. T., Myers, S., Fassnacht, C. D., Womble, D. S., Readhead, A. C. S., Blandford, R. D., & Pearson, T. J. 1998, *MNRAS*, 296, 483
- Jesseit, R., Naab, T., & Burkert, A. 2002, *ApJ*, 571, L89
- Keeton, C. R., Gaudi, B. S., & Petters, A. O. 2003, *ApJ*, 598, 138
- Kochanek, C. S. & Dalal, N. 2004, *ApJ*, 610, 69
- Koopmans, L. V. E., Biggs, A., Blandford, R. D., Browne, I. W. A., Jackson, N. J., Mao, S., Wilkinson, P. N., de Bruyn, A. G., & Wambsganss, J. 2003, *ApJ*, 595, 712
- Mao, S., Jing, Y., Ostriker, J. P., & Weller, J. 2004, *ApJ*, 604, L5
- Mao, S. & Schneider, P. 1998, *MNRAS*, 295, 587
- Metcalf, R. 2001, in *Where is the Matter?*, ed. L. Tresse & M. Treyer, (astro-ph/0109347)
- Metcalf, R. 2004, preprint, submitted to *ApJ*, astro-ph/0407298
- Metcalf, R. B. & Madau, P. 2001, *ApJ*, 563, 9
- Metcalf, R. B., Moustakas, L. A., Bunker, A. J., & Parry, I. R. 2004, *ApJ*, 607, 43
- Metcalf, R. B. & Zhao, H. 2002, *ApJ*, 567, L5
- Meza, A., Navarro, J. F., Steinmetz, M., & Eke, V. R. 2003, *ApJ*, 590, 619
- Moore, B., Ghigna, S., Governato, F., Lake, G., Quinn, T., Stadel, J., & Tozzi, P. 1999, *ApJ*, 524, L19
- Moustakas, L. A. & Metcalf, R. B. 2003, *MNRAS*, 339, 607
- Myers, S. T., Jackson, N. J., Browne, I. W. A., de Bruyn, A. G., Pearson, T. J., Readhead, A. C. S., Wilkinson, P. N., Biggs, A. D., Blandford, R. D., Fassnacht, C. D., Koopmans, L. V. E., Marlow, D. R., McKean, J. P., Norbury, M. A., Phillips, P. M., Rusin, D., Shepherd, M. C., & Sykes, C. M. 2003, *MNRAS*, 341, 1

- Patnaik, A. R. & Narasimha, D. 2001, MNRAS, 326, 1403
- Schechter, P. L. & Wambsganss, J. 2002, ApJ, 580, 685
- Schneider, P. & Weiss, A. 1992, A&A, 260, 1
- Sluse, D., Surdej, J., Claeskens, J.-F., Hutsemékers, D., Jean, C., Courbin, F., Nakos, T., Billeres, M., & Khmil, S. V. 2003, A&A, 406, L43
- Springel, V., Yoshida, N., & White, S. D. M. 2001, New Astronomy, 6, 79
- Trott, C. M. & Webster, R. L. 2002, MNRAS, 334, 621
- Zakharov, A. F. 1995, A&A, 293, 1